Unterschrift BetreuerIn

TECHNISCHE UNIVERSITÄT WIEN

DIPLOMARBEIT

Near-infrared hyperspectral single-pixel imaging system

zur Erlangung des akademischen Grades
Diplom-Ingenieur

im Rahmen des Studiums
Technische Physik

ausgeführt am Institut für
Angewandte Physik
der Technischen Universität Wien

unter der Anleitung von
Ao.Univ.Prof. Dr. Martin GRÖSCHL

in Kooperation mit der Firma
RECENDT GmbH

unter der Betreuung von
Mag. Jakob KILGUS

durch
Paul GATTINGER
Matr. Nr.: 01325326

Wien, 10. September 2019

Unterschrift StudentIn

Abstract

Single-pixel imaging via compressive sensing was introduced over a decade ago and has since then made an impressive leap forward. The possibility to sample signals, that show sparsity in a certain domain, below the Shannon-Nyquist sampling rate opens the ability to reduce data amounts whilst recording images with a single-pixel detector element. Combining single-pixel imaging with near-infrared spectroscopy opens a new, cost effective approach to hyperspectral imaging in the near-infrared domain, where molecular overtone vibrations can be exploited to perform chemical identification of samples. While common hyperspectral cameras in this wavelength region tend to be expensive and usually have to be cooled, this work presents a broadband (1500 nm - 2200 nm) hyperspectral near-infrared single-pixel camera built with simple and inexpensive parts, such as a digital micromirror device and a commercially available microspectrometer. In this thesis the developed setup is explained and several samples are investigated in order to characterize the performance of the hyperspectral single-pixel imaging system.

Zusammenfassung

Single-Pixel Imaging unter Verwendung von Compressive Sensing wurde vor über zehn Jahren erstmals beschrieben. Seither wurde diese Technik in zahlreichen Anwendungen implementiert. Die Möglichkeit Signale, die in bestimmten Domänen dünnbesetzt (Sparse) sind, unterhalb der Shannon-Nyquist Abstastrate zu samplen, ermöglicht es, Datenmengen während des Aufnehmens von Bildern mit Single-Pixel Detektoren zu reduzieren. Die Kombination aus Single-Pixel Imaging und Spektroskopie im nahen Infrarot eröffnet einen neuen, kostengünstigen Ansatz, um hyperspektrale Bildgebung in ebendiesem Wellenlängenbereich zu betreiben. Dies ist gerade auch deshalb interessant, da Moleküle dort Obertonschwingungen aufweisen, was zur zerstörungsfreien chemischen Analyse von organischen Proben ausgenutzt werden kann. Während herkömmliche hyperspektrale Kameras in diesem Wellenlängenbereich üblicherweise teuer sind und zudem gekühlt werden müssen, präsentiert diese Arbeit eine vergleichsweise kostengünstige, breitbandige (1500 nm - 2200 nm), hyperspektrale Single-Pixel Kamera für das nahe Infrarot. Die Kamera ist aus kommerziell erhältlichen Bauteilen, wie einem Digital Micromirror Device (DMD) und einem Mikrospektrometer aufgebaut. Im Folgenden wird auf das Konzept der entwickelten Hyperspektrale Kamera näher eingegangen. Ergebnisse aus Probemessungen werden präsentiert und zur Charakterisierung des bildgebenden Systems genutzt.

Acknowledgements

I would like to thank Jakob Kilgus as my main tutor, Ivan Zorin, Gregor Langer, Ramin Nikzad-Langerodi and Markus Brandstetter who supported this work with a lot of fruitful discussions and tips, Christian Rankl for his inputs concerning compressive sensing, Andrii Prylepa for some useful tips and discussions and Bettina Heise for lending me the DAQ-card and other useful laboratory items. Without the support of my family and my girlfriend Laura, this work would not have been possible. Last but not least I would like to thank Peter Burgholzer, CEO of RECENDT and Martin Gröschl, head of research unit "Applied and Computational Physics" at the institute of Applied Physics, TU Wien, for making this work possible at all.

Contents

List of Abbreviations

CV	**C**ross **V**alidation
DAQ	**D**ata **Ac**q**u**isition
DMD	**D**igital **M**irror **D**evice
DNA	**D**eoxyribo**n**ucleic **A**cid
DR	**D**ynamic **R**ange
FOV	**F**ield **O**f **V**iew
FPI	**F**abry-**P**érot **I**nterferometer
FTIR	**F**ourier-**T**ransform **I**nfra**r**ed
HDMI	**H**igh **D**efinition **M**ultimedia **I**nterface
IDCT	**I**nverse **D**iscrete **C**osine **T**ransform
LASSO	**L**east **A**bsolute **S**hrinkage and **S**election **O**perator
MEMS	**M**icro-**E**lectro-**M**echanical **S**ystems
MIR	**M**ear-**I**fra**r**ed
NIR	**N**ear-**I**fra**r**ed
PCA	**P**rinciple **C**omponent **A**nalysis
PSNR	**P**eak **S**ignal-to-**N**oise **R**atio
RIP	**R**estricted **I**sometry **P**roperty
SC	**S**uper**c**ontinuum
SNR	**S**ignal-to-**N**oise **R**atio

Chapter 1

Introduction

Compressive sensing was developed over a decade ago, allowing sampling of sparse signals below the Shannon-Nyquist rate [1]. The technique was subsequently applied in many fields where sparse signals are being processed. For example by the implementation of compressive sensing in atomic force microscopy [2], samples don't have to be scanned in their entirety any longer. Specific scanning patterns are sufficient for reconstructing atomic force microscopy images of the sample. In communications and networks [3] and wireless sensor networks [4] sparsity of signals can be exploited to reduce raw data amounts while still obtaining the full information. Another field is compressive spectroscopy [5], where optical multiplexing is achieved by using several transmission orders of a Fabry-Pérot interferometer, thus increasing the spectral range of the interferometer significantly.
The combination of spatial light modulators and single-element detectors leads to compressive single-pixel imaging [6], [7]. In 2006 Takhar et al. described the first compressive single-pixel imaging system that used a digital micromirror device (DMD) as a spatial light modulator. This technique enables imaging devices with only a single-element detector which usually has a high detectivity. This detector doesn't need to scan the sample because modulation of the scene is achieved by a DMD. Mathematical optimization algorithms allow high quality reconstruction of images at sampling rates that lie below the Shannon-Nyquist sampling rate under the condition that the recorded image is sparse in some domain. Practically this means that images of N pixels can be recorded with $M < N$ measurements. In the visible range of the electromagnetic spectrum many useful domains of single-pixel imaging have been highlighted. Radwell et al. [8] combined the single-pixel imaging technique with a microscope achieving frame-rates of up to 10 Hz and expanding the spectral range of the microscope into the near-infrared domain up to 1550 nm. Gustavsson et al. [9] presented a compressive sensing based telescope operating in the near-infrared domain and Soldevilla et al. [10] introduced a compressive sensing based polarimetric imaging system utilizing an analyzer.
The combination of compressive single-pixel imaging with spectroscopy enables hyperspectral imaging, where wavelength-dependent images of a sample are recorded. In recent studies hyperspectral single-pixel imaging has been demonstrated up to wavelengths of 1100 nm, using grating monochromators or fourier-transform interferometers as spectrometers [11], [12]. Shibuya et al. [13] pushed even further into the near-infrared domain by using a hyperspectral dual comb single-pixel imaging system covering a bandwidth of approximately 10 nm at a

wavelength of 1560 nm.
Hyperspectral single-pixel imaging is particularly interesting in the infrared domain where molecular vibrations reveal chemical information, thus making it possible to obtain spectral and spatial information about the sample. Therefore this technique has a variety of important applications such as non-destructive material testing. E.g. it has been shown, that hyperspectral near-infrared imaging systems can be used for blood detection at crime scenes without destroying the DNA [14].
Existing hyperspectral infrared camera systems based on focal plane arrays are usually very expensive and have to be cooled [15]. Additionally the photon efficiency of single-pixel detectors in combination with a DMD is higher than in conventional systems, because in every measurement 50 % of the DMD pixels illuminate the detector.
Aim of this study is to expand the technology of hyperspectral single-pixel imaging into the near-infrared domain. A broadband hyperspectral imaging system, based on the application of MEMS-based Fabry-Pérot microspectrometers, is presented. It operates in the wavelength range between 1500 and 2200 nm. The camera system is characterized by different test measurements on various test samples. The potential of extracting chemical and physical properties of different specimen is demonstrated by the utilization of data analysis algorithms. This approach is a proof of principle and it shows a compact and cost efficient alternative to conventional near-infrared hyperspectral imaging systems

Chapter 2

Methodology

2.1 Single-pixel imaging

An illuminated sample reflects incident radiation diffusely and gets imaged onto a DMD which encodes the image of the sample spatially by reflecting light from DMD pixels in the "on" position under a 24° angle. This part of the radiation gets collected by an optical system that focuses it onto a single-pixel detector element. Therefore, two dimensional images have to be constructed out of single-pixel measurement data points that are usually represented by a vector $\mathbf{y}$. The number of pixels of the resulting image, whose data points are represented in the vector $\mathbf{x}$, is determined by the number of pixels that are displayed on the DMD. Single-pixel imaging [7] enables image recording at very low sampling rates, meaning the number of elements in $\mathbf{y}$ is only a percentage of the number of elements in $\mathbf{x}$ which is usually around 10 to 20 percent.

Shannon-Nyquist sampling theorem

The Shannon-Nyquist sampling theorem states, that a signal $f(t)$ that contains no frequencies higher than B hertz can be represented entirely by discrete points spaced $1/(2B)$ seconds apart [16]. In other words: in order to measure a signal with a maximum frequency B without any losses it has to be sampled at twice this frequency.

Basics of compressive sensing

Compressive sensing evolved over a decade ago [1], [17] and it has revolutionized the way of signal processing. Exploiting sparsity of natural signals, such as images, it has become possible to acquire data below the Shannon-Nyquist sampling rate according to the following equation:

$$\mathbf{y} = \Phi\mathbf{x}. \tag{2.1}$$

In equation (2.1), $\mathbf{y}$ denotes the vector of the measured signals, Φ represents the sensing matrix and $\mathbf{x}$ is the original signal that is sparse in the domain Ψ, according to

$$\mathbf{x} = \Psi\boldsymbol{\alpha}, \tag{2.2}$$

where Ψ represents the transformation and $\boldsymbol{\alpha}$ are the sparse coefficients in the respective domain. In order to be sparse most of the coefficients $\boldsymbol{\alpha}$ have to be zero. The bandwidth B of the signal gets effectively smaller, due to those zero values. This illustrates why the sampling rate can be smaller than the Shannon-Nyquist rate. The new effective bandwidth B_{eff} is smaller than B and therefore the new, lower sampling rate is $2B_{\text{eff}}$.
In this work a two dimensional inverse discrete cosine transform (IDCT) was used as transformation operator Ψ. Sparsity of images under a discrete cosine transform can be assumed due to the successful application of the transform in image compression algorithms like JPEG [18]. To reconstruct the original signal $\mathbf{x}$ from a measured signal $\mathbf{y}$ an optimization algorithm has to be used. In this work a "least absolute shrinkage and selection operator with cross validation" (LASSO CV) has been employed [19].

$$\min\{\frac{1}{2M}\|\mathbf{y} - \Phi\Psi\boldsymbol{\alpha}\|_2^2 + \lambda\|\boldsymbol{\alpha}\|_1\}. \tag{2.3}$$

The LASSO algorithm (eq. (2.3)) is basically a least squares model with the constraint $\lambda\|\boldsymbol{\alpha}\|_1$, where $\|\boldsymbol{\alpha}\|_1$ is the regularizer and λ is the tuning parameter. M is the number of samples used to reconstruct the image. $\|.\|_1$ and $\|.\|_2$ denote the L_1- and the L_2-norm respectively. The L_1-norm in the regularizer forces the solution to be sparse, meaning that a vast amount of the components of the reconstructed signal are zero. To obtain a qualitatively good reconstruction a cross validation algorithm has to be used to find a good tuning parameter λ. The downside of the cross validation procedure is, that it is computationally expensive and therefore takes much longer than simply using a LASSO algorithm and choosing a tuning parameter by hand. But it is not likely to guess a good tuning parameter which justifies the utilization of LASSO CV. After optimizing the coefficients $\boldsymbol{\alpha}$ in the sparse domain, two dimensional IDCT is applied to transform the $\boldsymbol{\alpha}$ in order to obtain the reconstructed image.

Semi-Hadamard patterns

A Hadamard matrix H_n of size $N \times N$ with $N = 2^n; n \in N$, can be calculated subsequently using the definition of H_1 [20]:

$$H_1 = \begin{bmatrix} 1 & 1 \\ 1 & -1 \end{bmatrix}. \tag{2.4}$$

H_n can then be calculated using the following relation:

$$H_n = \begin{bmatrix} H_{n-1} & H_{n-1} \\ H_{n-1} & -H_{n-1} \end{bmatrix}. \tag{2.5}$$

The Hadamard matrices have entries 1 and -1, but the DMD only allows binary representations, because the micromirrors can be either in "on" or "off" position. This is where the semi-Hadamard matrices come into play. A Hadamard matrix gets split up into two matrices, setting either -1 or 1 to zero and taking

the absolute value of the remaining entries resulting in two semi-Hadamard matrices. For the Hadamard matrix in eq. (2.4) the two semi-Hadamard matrices would look like:

$$Hs_{1,1} = \begin{bmatrix} 1 & 1 \\ 1 & 0 \end{bmatrix}, Hs_{1,2} = \begin{bmatrix} 0 & 0 \\ 0 & 1 \end{bmatrix}. \tag{2.6}$$

Implementation of the semi-Hadamard patterns

The sensing matrix Φ consists of $M < N$ rows of the pseudo randomly permuted columns of H_n. Every measurement represents the multiplication of the signal coming from the sample $\mathbf{x}$ with one row of H_n. In order to be displayed on the DMD, each row has to be reshaped into a $\sqrt{N} \times \sqrt{N}$ array. Since the DMD can only represent binary patterns it is necessary to split each reshaped row, which consists of entries 1 and -1 into two respective binary arrays, called semi-Hadamard patterns, consisting of 0 and 1 entries. In the measurement process, the semi-Hadamard pattern pairs (Fig. (2.1)) are displayed consecutively. The two respective values that are measured with the single-pixel detector get substracted. The difference between those values represents the value that the full Hadamard matrix (with 1 and -1 entries) would have caused. The differential signal that results from M differential measurements, is represented by the vector $\mathbf{y}$. Besides being computationally efficient [21], this approach has an important benefit, namely neglecting thermal drifts that are slow compared to the displaying frequency of the patterns. An example of the resulting signal $\mathbf{y}$ is illustrated in Fig. (2.2).

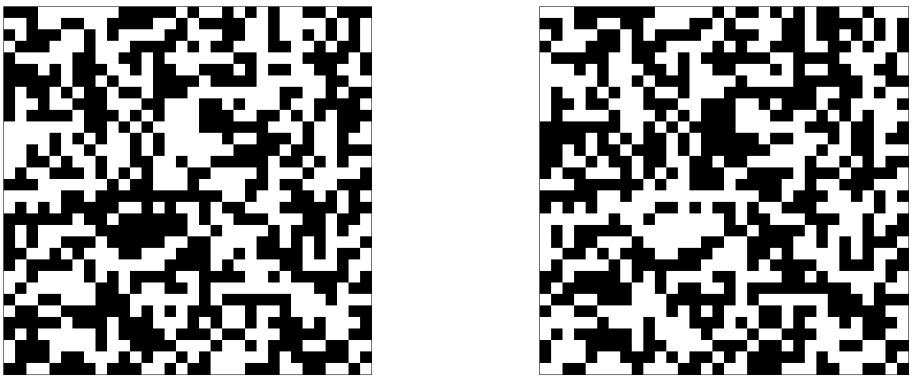

FIGURE 2.1: Two 32×32 pixel semi-Hadamard matrices that are used to encode the scene spatially via the DMD.

To guarantee that the matrix product $\Phi\Psi$ is suitable for a valid reconstruction, it has to fulfill the so-called restricted isometry property (RIP), first described by Candes et. al [22]. In general it is not possible to test $\Phi\Psi$ for fulfilling the RIP due to the fact that the underlying calculation is a hard combinatorial problem. In this work it is assumed, that the RIP is fulfilled due to the results that were obtained.

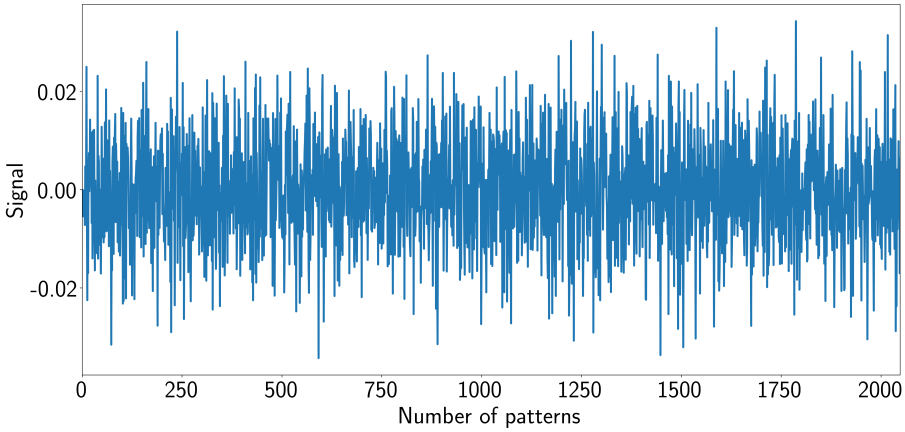

FIGURE 2.2: Differential signal that is obtained in a compressive single-pixel measurement.

Visualizing image reconstruction

In order to calculate an image from a signal shown in Fig. (2.2), an optimization algorithm is needed. In this work a LASSO CV (cross validation) algorithm (eq. (2.3)) implemented in the open source library scikit learn [23] was used to perform reconstruction. The LASSO CV algorithm calculates an optimal regularization parameter λ via cross validation, which is crucial for the minimization of eq. (2.3). The principle of cross validation is to divide the entries of the vector $\mathbf{y}$ into e.g. four subsets and optimize on three of them and then let the optimized model predict on the fourth part of $\mathbf{y}$ and the average error gets computed. This procedure is repeated for many different tuning parameters λ and ultimately a cross validation error curve is plotted as illustrated in (Fig. (2.3)). The optimal λ is the minimum of that curve. Fig. (2.4) shows the optimized $\boldsymbol{\alpha}$ coefficients of a 64×64 image in the sparse domain and the transformed image. Most of the pixel values in the left hand side image are zero (grey coloured). On the right hand side two dimensional IDCT was applied to obtain the reconstructed image. In this simulation the original image $\mathbf{x}$, seen in Fig. (2.5), was multiplied with the matrix Φ in order to obtain the signal $\mathbf{y}$. The number of rows of Φ is 2048, therefore the dimension of the vector $\mathbf{y}$ is also 2048, leading to a compression rate of 50 %. The left hand side of Fig. (2.5) illustrates the influence of λ on the reconstruction.

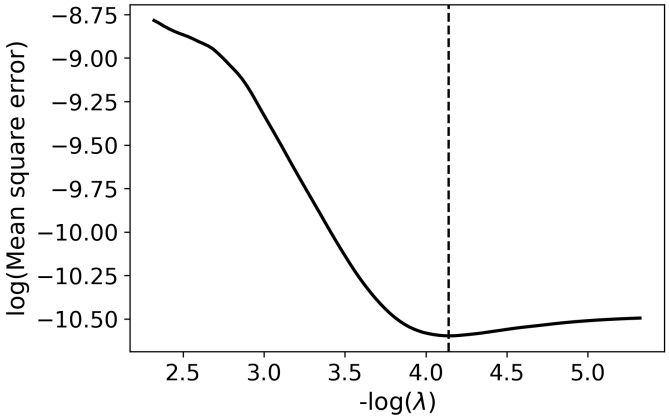

FIGURE 2.3: Mean square error of the cross validation for different tuning parameters λ.

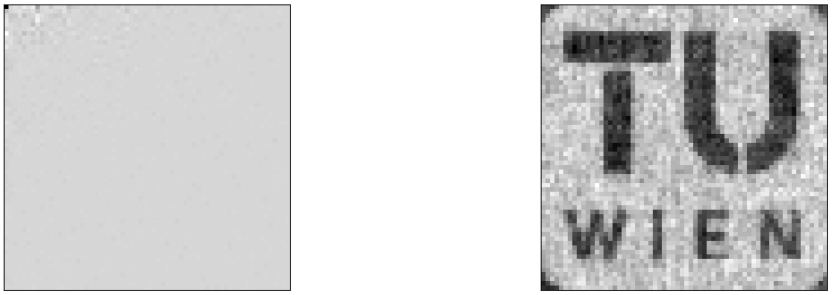

FIGURE 2.4: Left: reconstructed signal in the sparse domain; right: reconstructed signal discrete cosine transformed.

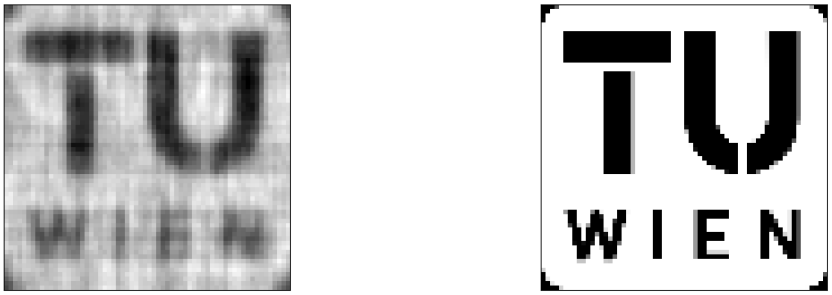

FIGURE 2.5: Left: reconstruction with a tuning parameter that is too big; right: original image used for the simulation.

2.2 Infrared spectroscopy

Transitions between molecular vibration modes can be induced by infrared radiation (Fig. (2.6)). Absorption bands in infrared spectra show those transitions between vibrational eigenstates of the molecules which can be approximated as sums of quantum mechanical harmonic oscillators. For example, a molecule

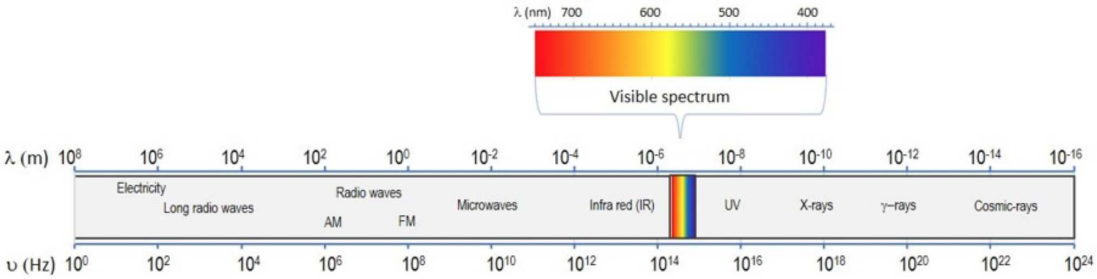

FIGURE 2.6: Infrared radiation is located between the visible radiation and microwave radiation in the electromagnetic spectrum. Image taken from [24]

consisting of two atoms can vibrate only in one direction. This can be illustrated by two masses that are connected by a spring. They can only oscillate along the axis of the spring. By increasing the complexity of a molecule (i.e. adding more atoms at different binding angles) the number of the vibrational modes increases according to $3N-6$, where N is the number of atoms that the molecule consists of and the number 6 stands for three translational degrees of freedom and three rotational degrees of freedom. This formula is only correct if non-linear atoms are considered, meaning that the binding angles between the atoms are not 180°. In the case of 180° binding angles, the formula $3N-5$ delivers the correct amount of vibrational modes, which can easily be verified for the aforementioned diatomic molecule. In this case the number 5 stands for three translational degrees of freedoms but only two rotational degrees of freedom, becaus rotation about the binding axis does not displace any atoms and therefore the dipole moment is zero. The vibrational modes of the molecules are quantized and for diatomic molecules one can approximate the eigenenergies according to the energy levels of a quantum mechanical harmonic oscillator.

$$E_n = h\nu(n+\frac{1}{2}) \tag{2.7}$$

In eq. (2.7) E_n represents the eigenenergy of the vibrational mode, n is the respective vibrational quantum number ($n=1,2,3...$), h is the Planck constant and ν is the frequency of the mode. This approximation is only valid for transitions of $\Delta n=1$ which are also called fundamental transitions. For transitions $\Delta n=2,3...$ (overtone transitions) anharmonic oscillator approximations have to be used (e.g. Morse potential). Fig. (2.7) shows the difference between the harmonic approximation and the Morse approximation of the potential energy of a diatomic molecule. E_n stands for the quantized energies of the molecule and E_d represents the dissociation energy that is needed to break the bond between the two atoms. The parameter r_0 is the distance between the two atoms in the energetic ground state E_0. For a harmonic potential those energies are equidistant whereas for the Morse potential the distances on the energy scale become gradually smaller while the average distance between the molecules becomes bigger for higher energies. For more complex molecules other methods,

such as simulations using a molecular Hamiltonian in order to describe the vibrational modes, are necessary. Fig. (2.8) shows a typical infrared spectrum of a polyethylene foil measured in a transmission setting. Three absorption bands between 2300 nm and 2400 nm can be seen which correspond to C-H overtone transitions between vibrational states of the polyethylene molecule. The absorbance is given by Beer-Lambert's law.

$$I(d) = I_0 e^{-\alpha d} \tag{2.8}$$

Where $I(d)$ is the intensity transmitted by the material, I_0 is the initial intensity, α is the wavelength-dependent absorption coefficient in m^{-1} and d is the thickness in m. The absorbance αd is calculated by manipulating Beer-Lambert's law:

$$\alpha d = -\log(I/I_0) \tag{2.9}$$

Different molecules have their distinctive transitions at specific energies making it possible to analyze the components of materials according to their infrared spectra [25].

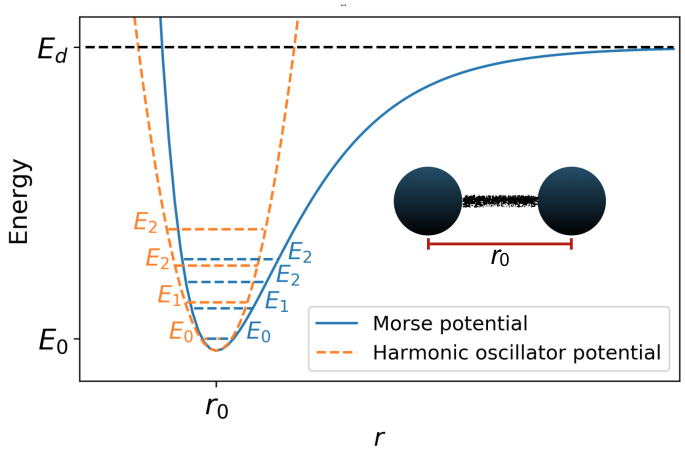

FIGURE 2.7: Harmonic approximation of a diatomic molecule vs. Morse approximation.

Spectroscopic methods

There are different methods to measure infrared spectra, three of them will be discussed here. Grating spectrometers use the angle dependent diffraction of different wavelengths. By rotating the grating different wavelengths can be measured. Fourier transform infrared (FTIR) spectrometers are usually based on a Michelson interferometer. The spectrum gets calculated via Fourier-transformation of the interferogram. Infrared spectra can also be measured by using Fabry-Pérot resonators combined with bandpass filters to suppress higher transmission orders of the Fabry-Pérot resonator. The transmission behaviour can be described via the following equation:

$$T(\lambda) = \frac{1}{1 + F \sin^2(\delta(\lambda)/2)} \tag{2.10}$$

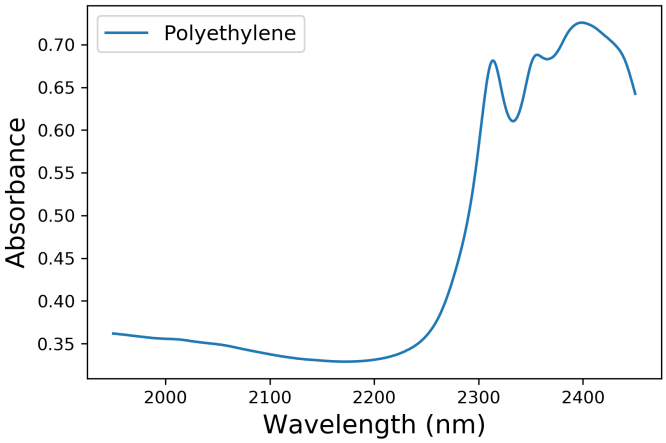

FIGURE 2.8: Infrared absorbance spectrum of a polyethylene foil.

where $T(\lambda)$ is the wavelength-dependent transmission, $F = 4R/(1-R)^2$ is the finesse as a function of the reflectivity R of the resonator mirrors and $\delta = 4\pi nd/\lambda$ is the optical thickness (for normal incidence), which is proportional to the distance d between the two mirrors of the Fabry-Pérot resonator. By varying d in Eq. (2.10), the transmitted wavelength can be selected as shown in Fig. (2.10), where the d_i stand for different mirror distances. The width of the peaks and therefore the spectral resolution is dependent on the reflectivity R of the mirrors and on the transmission order that is used. In order to obtain a spectrum, the transmission at different mirror distances d is measured and plotted against the wavelength.
Fig. (2.9) shows the working principle of a MEMS (Micro Electro Mechanical System) based Fabry-Pérot Interferometer (FPI). The size of the air gap d is varied by the applied control voltage. Additional bandpass filtering avoids the overlap of higher transmission orders that occur naturally in Fabry-Pérot filters. The spectral resolution of those miniaturized Fabry-Pérot filters is inferior to that of typical grating- or FTIR-spectrometers because they are much smaller. If the form factor was considered, the resolution would be equivalent. The small size of the microspectrometers and therefore a small d restricts the resolution. Additionally the reflectivity R should be chosen in a way that the SNR is still big enough. If R is near to 1, the peaks become sharper but the SNR drops. These restrictions of the mirror distance and the reflectivity is responsible for all of the common Fabry-Pérot microspectrometers having around 20 nm resolution in the near-infrared domain, while for example spectral resolutions less than 4 nm are possible with standard laboratory FTIR-spectrometers.

Spectral processing

Influences like varying room temperatures or changes in humidity can distort spectra. Scattering processes can also have influences on the data. In order to consider such effects and to interpret infrared spectra it is often necessary to process these spectra. Baseline correction [27] is a very powerful method to correct unstable baselines that often occur in spectroscopic data due to scattering,

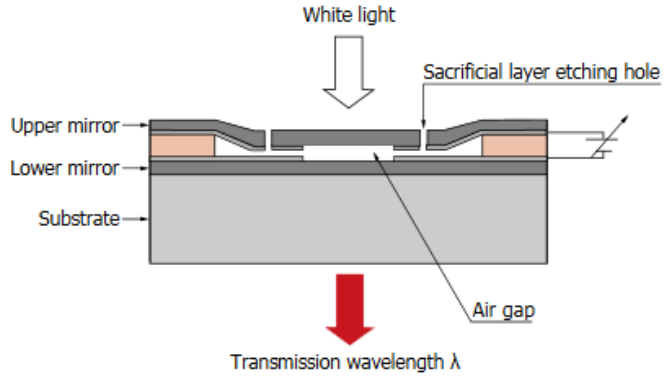

FIGURE 2.9: Scheme of a MEMS based Fabry-Pérot interferometer. [26]

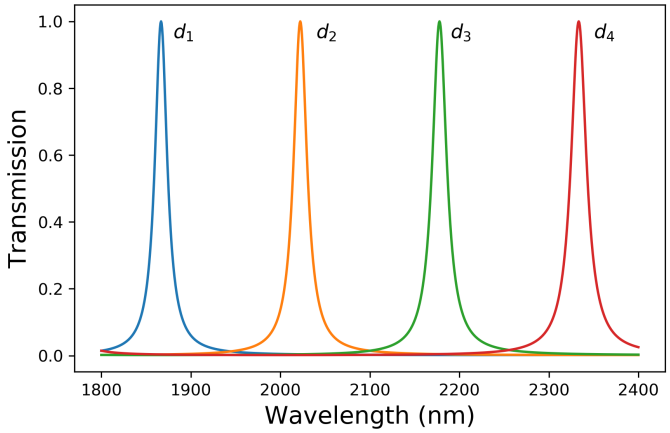

FIGURE 2.10: Transmission spectra of a FPI at different distances d_i between the mirrors.

noise or reflections.
Savitzky-golay filtering [28] is also commonly used to smooth out noisy data. These convolutional filters are easy to implement and standard in treatment of spectral data.

2.3 Hyperspectral imaging

By combining imaging with spectroscopy a further dimension is added resulting in hyperspectral imaging. Hyperspectral images are usually data arrays of three dimensions, the third dimension being the wavelength. Generally further dimensions such as polarization can be added to a hyperspectral data array. A hyperspectral image is commonly referred to as hyperspectral cube. All recorded images presented in this work are absorbance images for two reasons. Firstly, because we are dealing with spectroscopic information according to Beer-Lambert's law adapted for images:

$$A_p = -\log_{10} \frac{I_{p,i}}{I_{p,b}} \tag{2.11}$$

In eq. (2.11) A_p is the absorbance value of a single-pixel, $I_{p,i}$ and $I_{p,b}$ stand for the intensity value of the p-th pixel in the image (i) and for the intensity value of the p-th pixel of the background (b) measurement, respectively. And secondly, because some spectrometer dependent artifacts could be neglected by normalizing the measurement of interest onto a background measurement. If there are still artifacts, especially on the edges of the images, color scaling has to be applied. Artifacts are often high intensity valued pixels. If e.g. most of the pixels have regular values between 0 and 1 and an artifact has a value of 10, then the visual differences between the regular valued pixels will be suppressed. By color scaling those outliers can be neglected and the structure that the image shows becomes visible.

Image analysis

Data analysis can be beneficial for interpreting the huge amount of information that is contained in a hyperspectral cube. It is desirable to have a machine that is able to assign spectra to the corresponding material. In order to implement such a machine, statistical learning is useful to classify the data that results from hyperspectral images. The kind of algorithm used in this work is called logistic regression model [29]. It gets trained by a set of known test spectra and ultimately it should be able to classify spectroscopic data correctly. Of course it will only be useful to apply the model to the same kind of data it was trained on. Principle component analysis (PCA) [29] is used to reduce the dimensionality of a problem which helps visualizing the overlaps of different features of big datasets by eigenvalue decomposition of the so called correlation matrix of the dataset. In many cases it is possible to condense e.g. a 64 by 64 pixel by 60 wavelengths data cube into a two-dimensional scatter plot of the two dominant principal components including the most important information about the dataset. The evaluation of hyperspectral images was carried out using the orange toolbox, a freely available data analysis program [30].

Chapter 3

Experimental setup

A 35 W halogen lamp placed in front of a diffuser illuminates the sample which diffusely scatters the incident radiation that gets collected by an objective lens. The objective lens demagnifies and projects the image of the sample onto the DMD. Micromirrors (pixels) in the "on" state reflect the incident radiation through a focusing system towards the microspectrometer which consists of a Fabry-Pérot tunable filter and a single-pixel detector (Fig.(3.1) and Fig.(3.2)).

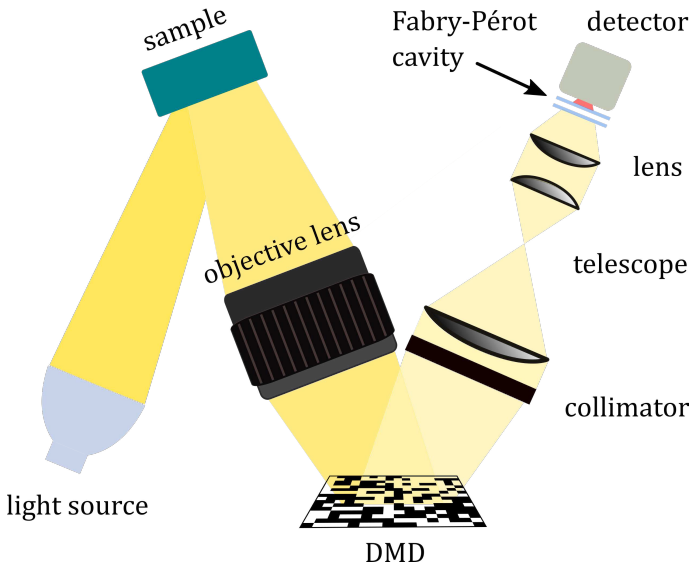

FIGURE 3.1: Experimental setup of the hyperspectral single-pixel camera [31].

Illumination

There are two main requirements for near-infrared light sources for the application of single-pixel imaging. On one hand the source has to emit sufficient radiation in the NIR to obtain a good signal-to-noise ratio (SNR) but on the other hand it should not burn the sample. Furthermore the angle of the incident radiation is important because of following reasons. Specular reflection should be avoided since the surface of the sample has to be perfectly flat, which is rarely the case. If the surface is not perfectly flat, only parts of it will be specular reflecting towards the objective lens. Those parts of the surface, that

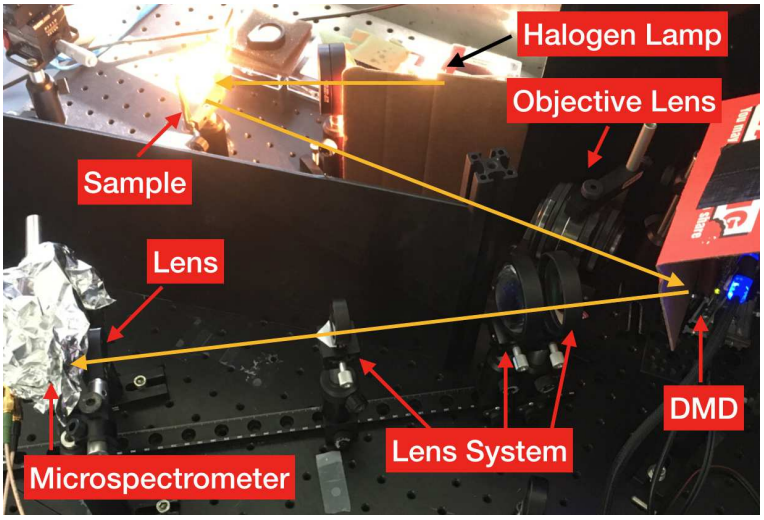

FIGURE 3.2: Photograph of the setup of the hyperspectral single-pixel camera.

are specular reflecting, yield very high intensities in the resulting image. This makes spatial chemical analysis difficult, because the same material could show huge intensity differences in different areas of the image. Nevertheless, the wavelength-dependent behaviour would still be the same. In addition specular reflection leads to imaging the light source rather than the sample, although this issue can be overcome by normalizing the measurement to a background measurement. Scattered electromagnetic radiation of surfaces that are not perfect diffuse scatterers (non-Lambertian surfaces), has an angular dependence and therefore a diffuse reflection setup with a rather steep incident angle is preferred. In this study a 35 W halogen lamp (International Light Technologies, L514-G) was used.
Additionally a supercontinuum (SC) source [32] (NKT Photonics, SuperK MIR) with an emission spectrum shown in Fig.(3.3) was used to show its potential concerning spectral power and spatial coherence. The power is so high that spectral filters have to be placed in front of the sample in order to avoid destruction. Measurements in combination with a bandpass filter and a standard infrared detector were made. Supercontinuum emission can be produced using femto second pulsed lasers in combination with highly nonlinear optical fibers such as chalcogenide fibers [33]. SC-sources usually have a high spatial coherence but show no phase coherence due to their broad spectrum.

Imaging optics

In a conventional camera system the image has to be projected on the camera chip or film. In the case of single-pixel imaging the film or chip is replaced by the DMD, hence projections on the DMD have to be sharp in order to obtain sharp images. The optical system used for imaging the sample onto the DMD has to fulfill several criteria. It should not show any unwanted effects like spherical or chromatic aberration and it should be designed for the given circumstances

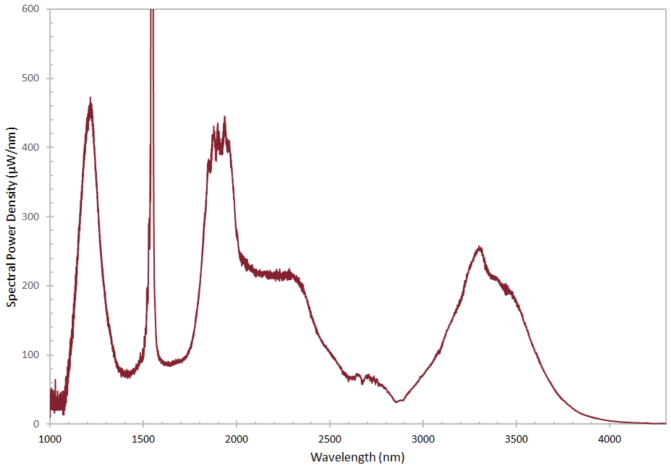

FIGURE 3.3: Emission spectrum of the supercontinuum source, taken from [34]

(e.g. Telephoto lens or microscope lens system). In addition, the optical system should be transparent for near-infrared radiation. In the experimental setup these requirements were fulfilled by using a Helios 44-2 camera objective lens, with a focal length of 58 mm in the visible range of the spectrum and a lens speed of $f/2.0$ to $f/16$.

Digital mirror device (DMD)

The essential part of a single-pixel imaging device is the DMD serving as a spatial light modulator. It consists of micromirrors on a silicon substrate that can be tilted about an axis. Fig. (3.4) shows the three different states of a single micromirror: the flat-state-position, the on-state-position and the off-state-position. The maximum switching rate between on-state and off-state-position determines the maximum rate at which binary patterns can be displayed on the DMD. The DMD used in this work (Texas Instruments, DLP4500) has a maximum switching rate of 2880 Hz and consists of 1140*912 micromirrors. This rate could not be exploited in the experimental setup. Since the DMD was operated as a second monitor at a 60 Hz frame rate, the maximum possible frame rate would have been 1440 Hz. The controlling script could only load one semi-Hadamard pattern per frame. This led to a maximum possible display rate of 60 Hz. Due to the DMD's window material, that protects the micromirrors, its use is restricted to the near-infrared domain only (up to 2500 nm).

Focusing optics

The lenses used in this work were N-BK7 glass lenses with different diameters and focal lengths. For collimation of the incident radiation, a 2 inch, $F = 60$ mm lens (Thorlabs) was used. The focusing optics consisted of two 2 inch lenses with $F = 150$ mm and $F = 60$ mm and two 1 inch lenses with $F = 40$ mm and $F = 30$ mm (Thorlabs). A second, shorter variant of the focusing system

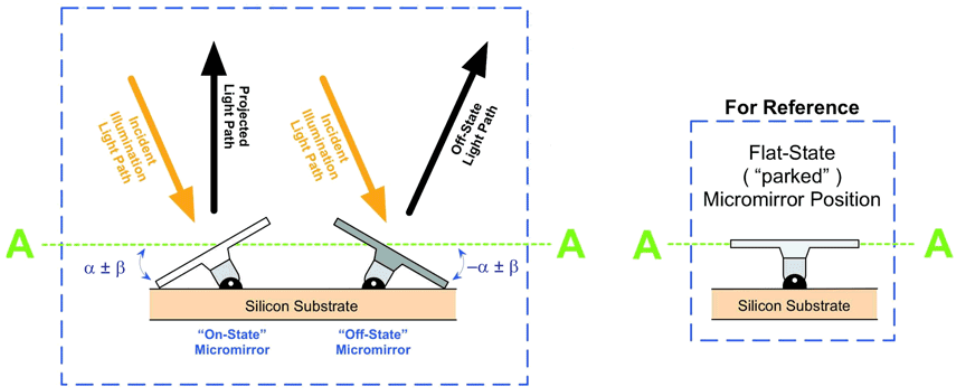

FIGURE 3.4: Working principle of the DLP4500 [35].

consisted of only two lenses, one with 25 mm diameter and $F = 60$ mm and the other one with 12 mm diameter and $F = 15$ mm focal length (Edmund Optics). A crucial task was to project the intermediate image with a width of 8 mm produced on the DMD onto the single-element detector with an effective detector area of 0.3 mm. Therefore an optical system with a demagnification of 27 is needed. Two simulations of the focusing optics have been generated using the commercial optical simulation program ZEMAX. It is essential to guide a sufficient amount of light to the detector in order to achieve a high SNR, hence aperture sizes should not be too small. As seen in Fig. (3.5), the length of the whole system is quite big and parts of the intensity (beam radius at detector: 0.49 mm) are cut by the detector aperture which is only 0.3 mm in diameter at an overall system length of 824 mm and an aperture diameter of 3 mm. Nevertheless, sufficient intensity could be collected to produce the hyperspectral images shown in this work. As an alternative (Fig. (3.6)) simulations with a shorter distance between the DMD and the microspectrometer were made. On the one hand a bigger demagnification can be achieved by using lenses with shorter foci, on the other hand aperture sizes in the optical system have to be smaller which again leads to intensity loss. This alternative focusing system would lead to a beam radius at the detector of 0.25 mm, so only little parts of the intensity would be cut by the detector aperture. Additionally this system would have an aperture size of 1.8 mm and an overall length of only 466 mm which makes this variant 358 mm shorter than the first one. The field of view of both variants was assumed to be 24 mm by 24 mm. The alternative system was tested in combination with a supercontinuum source (Fig. (3.7)).

Microspectrometers

MEMS-FPI microspectrometers offer an alternative to the much bigger and more expensive FTIR spectrometers. However standard FTIR spectrometers still have a better spectral resolution, which makes them inevitable for specific tasks. MEMS-FPI microspectrometers are very small (Fig. (3.9)) and due to their compactness, robustness and the possibilities of data processing, they can

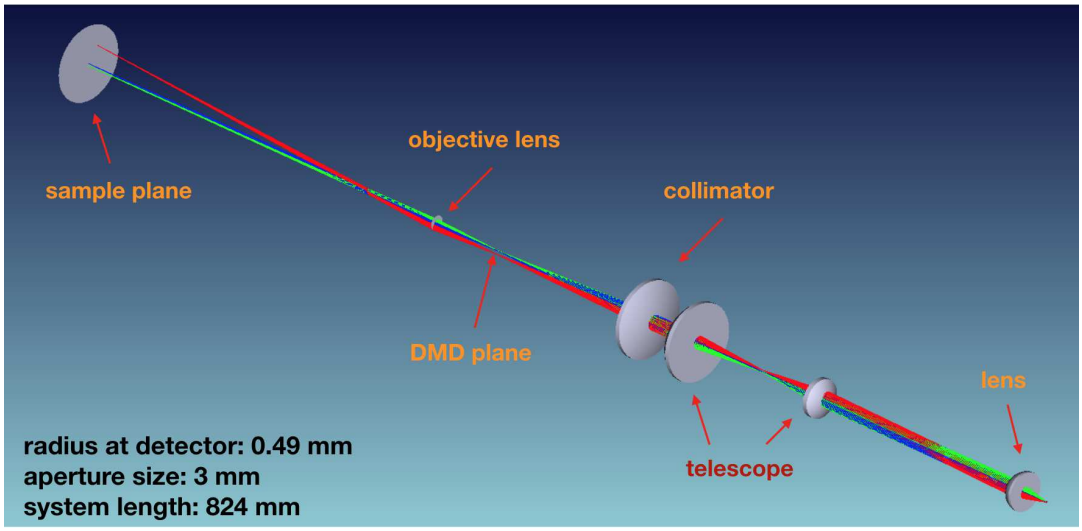

FIGURE 3.5: ZEMAX simulation of the experimentally realized setup. Note that the beam radius at the detector is larger than the detector aperture.

be used in many applications where smaller spectral resolutions are sufficient. Different MEMS-FPI microspectrometers (C14273 and C13272-02, Hamamatsu and NIRONE 2.0, Spectral Engines) were used as single-pixel detectors. The NIRONE spectrometer is a fully integrated product with a communication script provided by the producer. Sending a measurement command from the software to the spectrometer takes roughly 2 s. This results in acquisition times of 68 min for a 64 by 64 pixel image with a compression rate of 50 %. This is the reason why this spectrometer was not used furthermore.
The Hamamatsu spectrometers in contrast are not fully integrated and therefore have to be used in combination with an amplifier a filter driver and an external DAQ-card, thus leaving more options to the user. Additionally the Hamamatsu microspectrometers do not have any pre-installed lenses in front of the Fabry-Pérot tunable filter (FPTF), making it possible to put them into the optical path of the single-pixel imaging system without exchanging any lenses of the setup. Both the C14273 and the C13272-02 consist of a bandpass filter, an FPTF (Fig. (3.9,3.10)) and an InGaAs detector. The wavelength range of the C14273 and the C13272-02 is 1750 nm-2150 nm and 1550 nm-1850 nm respectively. Maximum spectral resolution of both spectrometers is 20 nm and the time constant is 1 ms. The filter control voltage was applied by a filter driver and the corresponding wavelengths were determined by solving a 5^{th}-order polynomial equation including temperature compensation factors provided by Hamamatsu. Fig. (3.8) shows the connection between the control voltages and the transmitted wavelengths.

Amplification and data acquisition

An amplifier (Femto, DLPCA-200) with 10^9 amplification and a lowpass filter of 10 Hz fed the signals to the 16 bit DAQ-card (Measurement Computing, USB-1608FS-Plus) with a maximum sampling rate of 100 kHz. For the measurements

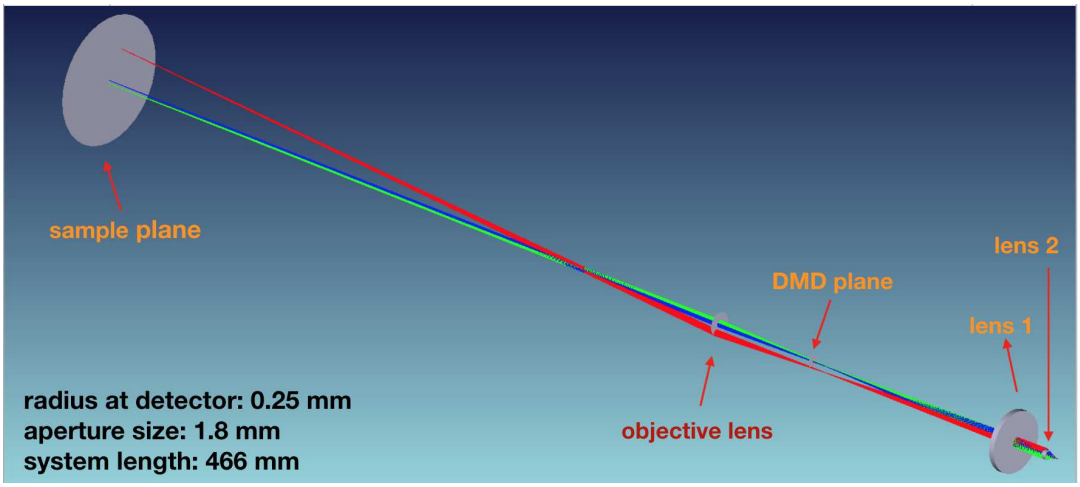

FIGURE 3.6: ZEMAX simulation of a shorter variant of the setup. The radius of the beam at the detector is smaller but still bigger than the aperture size of the detector.

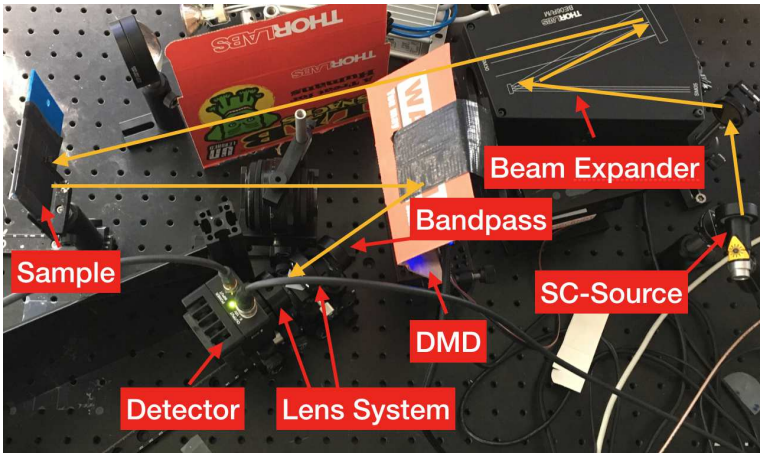

FIGURE 3.7: Setup of the short variant. A supercontinuum source was used for illumination.

presented in this work, a 10 kHz sampling rate was used.

Python script and synchronisation

The measurement process was controlled by a script written in Python using the package Pyqtgraph which is based on Qt. The DMD was used as a second monitor via HDMI connection where the semi-Hadamard patterns were displayed using an event loop written with Pyqtgraph. For each displayed pattern 50 data points were sampled with the 16 bit DAQ-card operating at 10 kHz in 1 V mode. The raw data was stored and further manipulation was carried out in post-processing. After displaying the whole set of predefined patterns, the filter driver received a signal to move the Fabry-Pérot filter to the next position. This process was repeated until all the wavelengths of interest were covered. Due to the fact, that the DMD offers no trigger signal when operating via HDMI connection, it was not possible to display the patterns at higher rates than 10 Hz

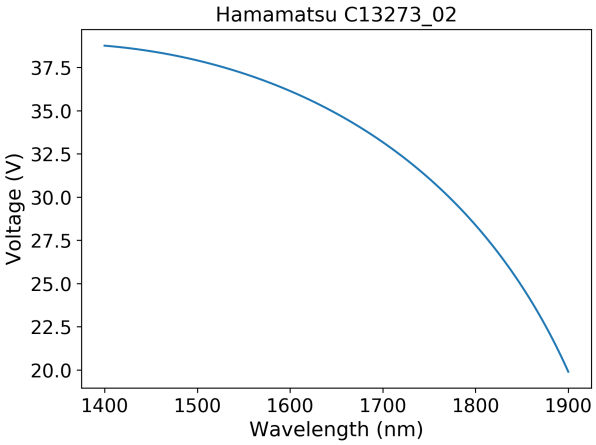

FIGURE 3.8: Connection between the control voltage applied to the Fabry-Pérot tunable filter and the transmitted wavelength.

FIGURE 3.9: Left: size of the Fabry-Pérot tunable filter chips; right: size of the whole microspectrometer.

which lead to measurement times of 4 min for e.g. a 50 percent compressed raw intensity image at a single wavelength.
There are two ways to improve the speed of a measurement. Storing the patterns on the internal memory of the DMD could eliminate latencies. These latencies occur due to the fact, that the patterns are plotted via a python command. In this approach the DMD would not be used as a second monitor and therefore trigger signals could be obtained. Alternatively a synchronization method for the use of the DMD via HDMI connection was introduced by Welsh et. al. [36]. Where the 24 colour bit-planes of each frame of the DMD were exploited. In each frame synchronization patterns (e.g all mirrors in "on" position, leading to a high signal) can be built in, leaving 22 remaining useful planes within the frame to display 11 inverse pattern pairs. This leads to theoretical pattern display rates of 660 Hz making acquisitions at a rate of 1 Hz possible (for 64 by 64 pixel images) with the DMD used in this work.

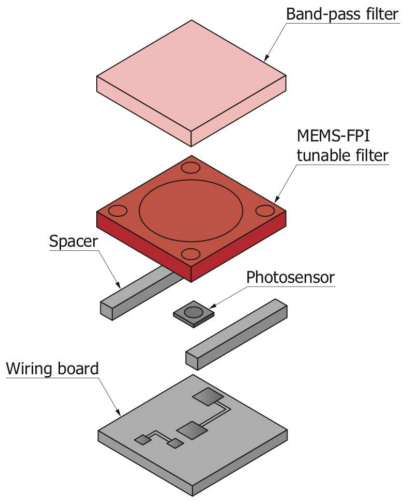

FIGURE 3.10: Structure of a Hamamatsu NIR microspectrometer [26].

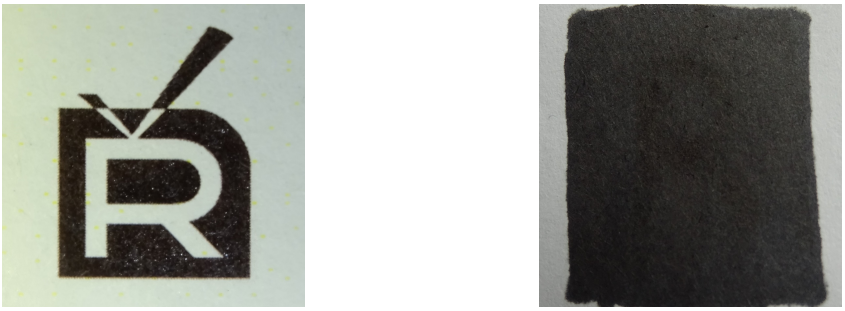

FIGURE 3.11: Left: Photograph of the printed logo on white paper; right: Black letter R drawn with an edding 360 marker overpainted with an edding 3000 marker.

3.1 Samples

Black R printed on white paper

An icon was printed with black toner on a white standard office paper (Fig. (3.11) left). This sample was used to characterize the reconstruction quality as seen in chapter 4.

Markers

Two different markers were utilized to produce a sample for demonstrating thermal imaging. Marker 1 (edding 3000) was used to overpaint the letter "R" written with marker 2 (edding 360) on white paper (Fig. (3.11) right).

Glues on textile substrate

Four different glues of the following brands and main active components were deposited on a piece of green textile (65 % polyester, 35 % cotton) taken from

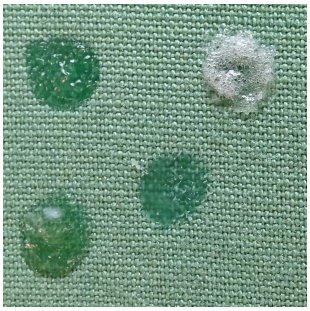
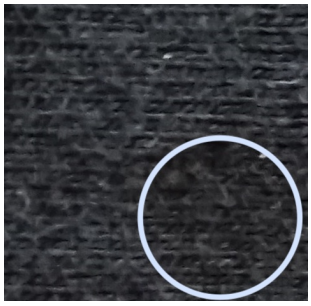

FIGURE 3.12: Left: photograph of the four different glues on the cloth substrate; right: photograph of a bloodstain (highlighted) on black cloth substrate

a shirt (shown in Fig. (3.12) left):
1.) "Loctite Power Flex" - ethyl-2-cyanoacrylate
2.) "UHU Alleskleber" - ethanol, acetone
3.) "Pattex Kraft Mix" - epoxy
4.) "RS Superglue Gel" - ethyl-2-cyanoacrylate

Blood on textile substrate

A drop of blood from the "Blutspendezentrale Wien" was transferred onto a piece of black cloth (95 % cotton, 5 % viscose), as seen in Fig. (3.12).

Chapter 4

Characterization

Raw signal

The whole system is noise-limited by the InGaAs detector integrated in the Hamamatsu spectrometer. Also the DMD could add to the system noise since it brings in extra frequencies due to the mirror flipping that happens at frequencies up to 1440 Hz. Fig.(4.1) shows the fourier transform of the signal that is detected by the microspectrometer during the measurement process. The signal was sampled by a Teledyne Lecroy Oscilloscope. One can clearly see a prominent peak (zoom factor 70) centered around zero, resulting from the fact, that there signal shows only tiny variation and is more or less a constant resulting in this prominent peak in Fourier space. Higher peaks are also visible at 60 Hz and all multiples of 60 Hz that result from the mirror flippings at 60 Hz frame rate predetermined by the HDMI connection. The higher multiples indicate the additional flippings happening within each frame. Those are representing the 24 colour (8 channels for each color) channels of the DMD.

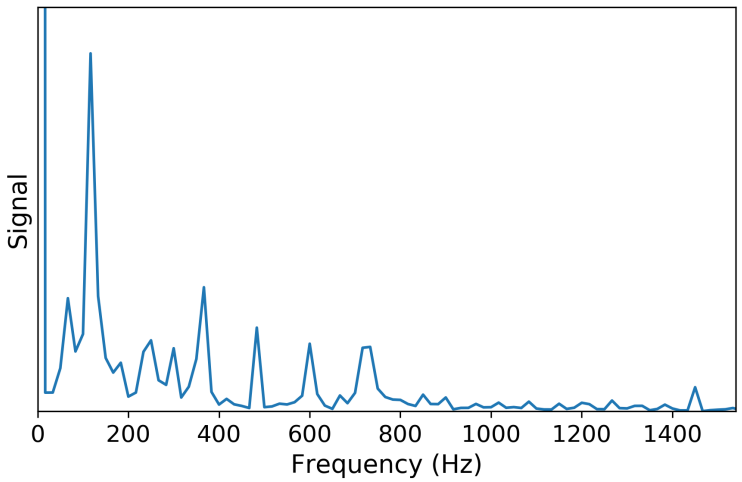

FIGURE 4.1: Fourier transform of the raw signal measured by the microspectrometer; only 1/70 of the first peak is shown.

Field of view

The field of view (FOV) is the physical size of the area that is imaged. Depending on the distance between the camera objective lens it can vary. The FOV of all the measurements made in this work is 24 mm by 24 mm.

Dynamic range

The dynamic range (DR) of a system is usually specified by the maximum and minimum possible value it can produce.

$$\mathrm{DR} = 20 \log_{10} \left(\frac{P_{\max}}{P_{\mathrm{noise}}} \right) \tag{4.1}$$

Since this work is presenting absorbance images, in eq. (4.1) $P_{\max}$ is the maximum possible absorbance value. A good approximation to this value is measured by covering the detector, which yields nearly 100 % absorption (only detector noise is taken into account). The background measurement was performed on white paper, which is highly reflective in the NIR.

$$P_{\max} = -\log_{10} \left(\frac{I_{\mathrm{air}}}{I_{\mathrm{paper}}} \right) \tag{4.2}$$

I_{air} in eq. (4.2) is the mean intensity value of all the pixels resulting from a measurement with no sample (only air) in the sample compartment. I_{paper} is the mean value over all pixels from a measurement of white paper. P_{noise} is the standard deviation of the signal that was calculated by measuring the two dimensional equivalent of a hundred percent line which is a common practice in infrared spectroscopy [25].

$$P_{\mathrm{noise}} = \mathrm{std} \left(-\log_{10} \left(\frac{I_{\mathrm{b1}}}{I_{\mathrm{b2}}} \right) \right) \tag{4.3}$$

In eq. (4.3) I_{b1} and I_{b2} are not mean values. $I_{\mathrm{b1}}/I_{\mathrm{b2}}$ has to be understood pixel-wise. Each pixel value of the first measurement gets divided by the value of the corresponding pixel in the second background measurement. std stands for the standard deviation of the array of values that $-\log_{10}(I_{\mathrm{b1}}/I_{\mathrm{b2}})$ produces. As background white paper was used. The dynamic range for a zero compression measurement at a wavelength of 2190 nm was 43 dB and for 90% compression it was 40 dB.

Peak signal to noise ratio (PSNR)

In the field of imaging, the PSNR is commonly used to determine the amount of noise in compressed (e.g. JPEG) images. Therefore the PSNR can be used to evaluate the reconstruction quality in single-pixel imaging. For the calculation of the PSNR eq. (4.4) was used, where $P_{0,i}$ stands for the values of the pixels of a zero compression image, and $P_{r,i}$ represents the pixel values of the reconstructed image at a compression rate r.

$$\mathrm{PSNR} = 20 \log \left(\frac{P_{\max}}{\sqrt{\sum_{i=1}^{N} (P_{0,i} - P_{r,i})^2}} \right) \tag{4.4}$$

In order to evaluate the reconstruction quality, PSNR values were calculated in dependence of the compression rate.

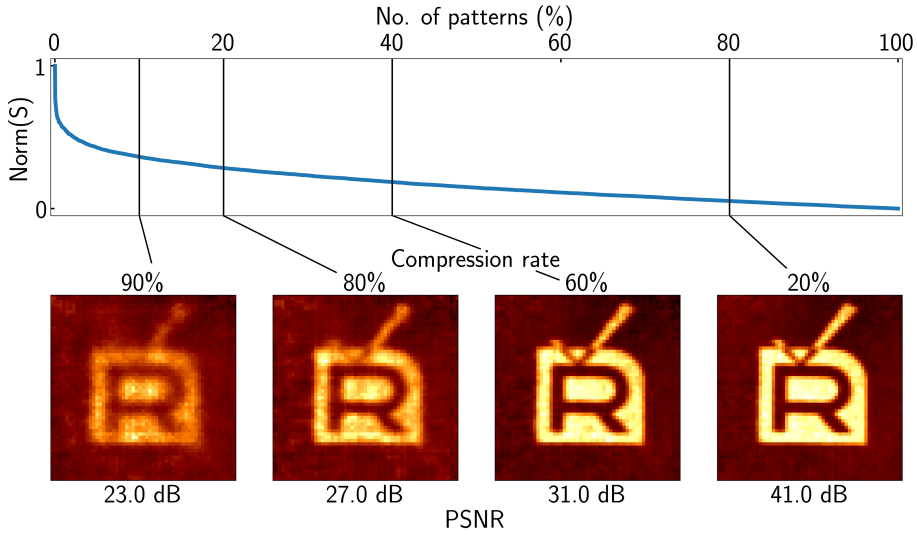

FIGURE 4.2: Data points ordered according to their absolute values; PSNR at different compression rates.

In Fig. (4.2) the top plot shows differential values of a zero compression measurement. The data points are rearranged in descending order according to their absolute values. By using only ten percent of the data points (i.e. 90% compression) with the biggest values, a well recognizable image of the logo printed with black toner on white paper was obtained. By reducing the compression rate further, the images become sharper and less noisy. It also turns out, that neglecting the first 10 percent of the signal (i.e. the highly contributing values) and using only the remaining 90 percent of the signal leads to a failing reconstruction. At least a few data points with high differential values are necessary for a successful reconstruction. These differential values result from applying the semi-Hadamard pattern pairs. Every pattern is followed by its inverse (all mirrors change their state to the opposite). Each value in the ordered signal in Fig. (4.2) is the difference in intensity of two corresponding semi-Hadamard patterns. The failing of the reconstruction by neglecting the highest differential values seems somehow plausible, since big differential values mean, that many of the illumination mask pixels, that are in the "on state", are close to an edge between highly scattering and absorbing medium. This means that frames that deliver high values contain information about the contours of the sample.

It is possible to use this insight to improve reconstruction quality of hyperspectral cube measurements. The very first measurement (e.g. at the biggest wavelength) could be carried out using the full set of Hadamard patterns (0% compression). Then the semi-Hadamard pattern pairs corresponding to the

biggest differential values could be filtered. For the remaining measurements at different wavelengths only those patterns could be used. This approach would make the following measurements highly compressive. This strategy only works if it can be assumed, that the overall contour of the sample does not change drastically over the measured spectral bandwidth. If the contours change, then the highest differential values for one wavelength may not be the highest differential values for another wavelength and the reconstruction quality could decrease or even fail.

Speed

The recording time of a 50 % compressed image data set takes about 3.8 min and is theoretically limited by the frame rate of the monitor (the DMD was used as second monitor of a PC). Due to software indicated latencies and the lack of analog triggers, the maximum possible switching rate of the Hadamard masks was 10 Hz. Using the internal memory of the DMD system and wrapping the binary Hadamard masks into the bit planes of a respective frame could reduce measurement times drastically [36], [37] as explained more detailed in chapter 3.

Chapter 5

Results and discussion

First measurements with the Hamamatsu microspectrometers

Before the first samples could be measured, the setup had to be adjusted. First results of those measurements can be seen in Fig. (5.1). It shows an image of the word “Pi” (Raspberry Pi package; black toner on cupboard) at a wavelength of 1820 nm. It is a 64 by 64 pixel measurement with a clearly visible artifact in the upper right corner. Those artifacts occur where the circular shaped aperture blocks the infrared radiation and therefore the reconstruction algorithm assigns values close to zero to those areas, which is basically noise. The background image shows the same effect: in the region of the aperture the pixel values are representing detector noise. All the absorbance images are the result of applying eq. (2.11) pixelwise. If the ratio of two values in the region of the aperture delivers very small numbers, the negative logarithm of those small values leads to high absorbances, as seen in Fig. (5.1).

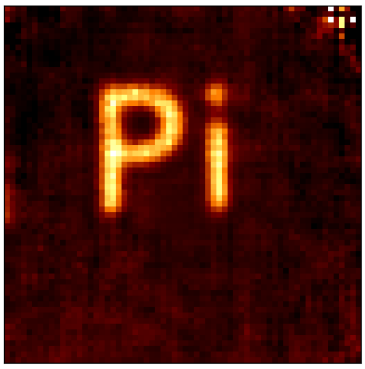

FIGURE 5.1: Image of the letter Pi at 1820 nm recorded with a Hamamatsu C13272-02 microspectrometer.

5.1 Different markers

In order to demonstrate the advantage of imaging in the near-infrared domain, measurements of the sample "markers", described in chapter 3, were made. Spectral imaging at two wavelengths was carried out. Fig. (5.2) shows the

absorption images at the respective wavelengths (1822 nm and 1772 nm). These wavelengths were chosen because the spectra obtained in a measurement using a laboratory FTIR spectrometer showed differences in absorbance at those two wavelengths. While hardly perceivable in the visible region of the electromagnetic spectrum there is a noticeable contrast between the two markers in the NIR region. But there is no difference between the absorption intensities of the two different markers at the two respective wavelengths. The absorption intensities seen here are most probably resulting out of the layer thicknesses and do not represent the spectral information. Overpainting leads to much thicker paint layers in the region of the letter R resulting in higher absorption according to Beer-Lambert's law (eq. 2.8). Again artifacts in the corners of the images arise. The explanation why these artifacts occur is the same as mentioned above.

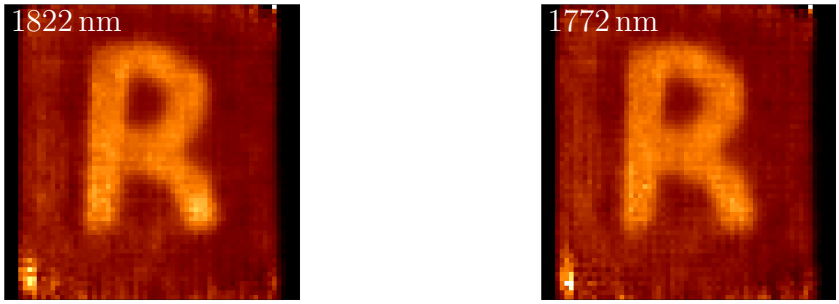

FIGURE 5.2: Left: image of the letter R written with marker 1 and overpainted with marker 2 at 1822 nm; right: measurement at 1772 nm

5.2 Hyperspectral analysis of adhesives on cloth substrate

The potential of hyperspectral imaging in the near-infrared could be shown by measuring the sample "glues on textile substrate". Absorbance images were recorded at 60 different wavelengths between 1550 nm and 1850 nm. The whole process of recording those images was divided into two parts. Firstly, background measurements of only the textile were carried out. Secondly, the adhesive samples on the substrate were measured. A single wavelength measurement took approximately 4 min. Therefore the total time of both background and sample measurement for the complete wavelength range took about 480 min. Reconstruction per intensity image took approximately 50 s. Total reconstruction time therefore took approximately 50 min on a standard office PC. Using the orange toolbox, spectra were extracted pixelwise. Those spectra were baseline corrected and Savitzky-Golay filtered. Principal component analysis was carried out and a logistic regression model was trained to classify the data.

Fig. (5.3) shows the baseline corrected and Savitzky-Golay filtered spectra that were extracted pixelwise from the absorption images. For better illustration the spectra are presented in a stacked way. This is why absorbance values of the

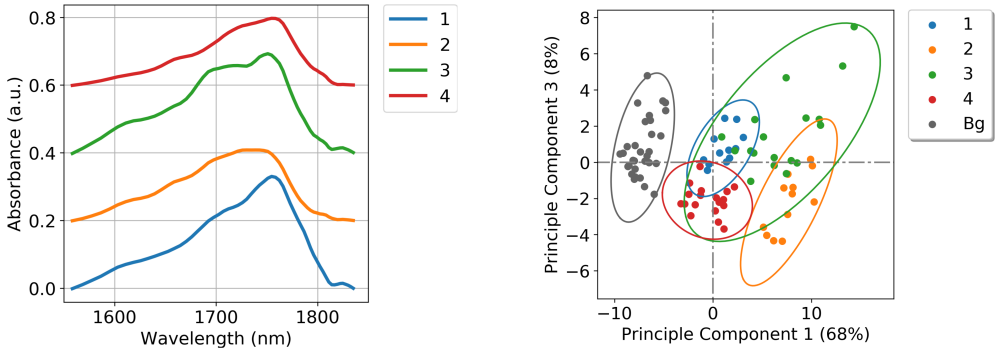

FIGURE 5.3: Left: Extracted spectra of the glues from a hyperspectral measurement; right: Principal component analysis of the hyperspectral datacube.

stacked curves are shifted and therefore not representative. The right side of Fig. (5.3) shows principal component 1 plotted against principal component 3. It is clearly visible, that the principal components of the different glues are strongly overlapping. This is resulting from spectral similarities. Additionally, due to the surface structure of the adhesives it is possible, that wavelength-dependent scattering occurs, which is distorting the spectra. However, adhesives 1, 2 and 4 as well as the background are separated well by applying PCA.

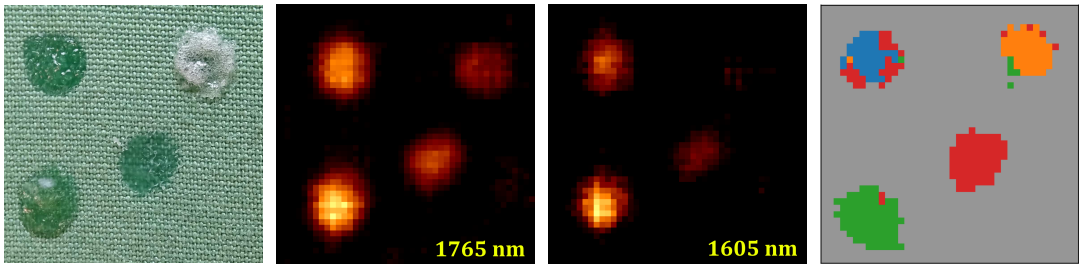

FIGURE 5.4: Left: photograph of 4 different glues on a cloth substrate; middle left: image of the different glues at 1756 nm; middle right: image of the different glues at 1605 nm; right: false colour image produced by the logistic regression model.

In Fig. (5.4) a photograph of the samples is shown. Two absorption images at distinctive wavelengths 1756 nm and 1605 nm illustrate that the intensity of the glue stains is wavelength-dependent. It is noticeable, that at the lower wavelength image, two of the adhesives are hardly visible anymore. The right hand side of Fig. (5.4) shows a false color image produced by the logistic regression model. The model was trained by selecting a small amount of pixels of each stain and assigning them to the respective adhesive. The remaining pixels were assigned by the model. It is possible to determine the background from the adhesives and also adhesive 4 is well separated. The logistic regression model leads to a similar conclusion as the PCA. It is not possible to separate the different adhesives completely. This is due to the fact that the samples are not perfectly homogeneous and flat. It is not achievable to apply equally thick layers of adhesives to the cloth and especially at the borders the layers get

thinner. This leads to less intensity in those areas which can be explained with Beer-Lambert's law. Furthermore the surfaces of the glue layers are not plain. Therefore scattering effects and specular reflection could be very prominent and distort the spectra.

5.3 Hyperspectral analysis of blood on cloth substrate

Detecting small blood stains on dark materials such as black clothes is possible by applying luminol. This common technique is used in crime scene investigations but its disadvantage is, that the DNA contained in the blood could be destroyed. Hyperspectral imaging is an interesting alternative to this approach. The spectra of the stains could be extracted from the data cube and via data analysis, the presumed blood stains could be verified. This experiment shows the capability of the hyperspectral single-pixel imaging setup to detect blood stains. The black cloth sample containing a blood stain was measured at 55 different wavelengths with the Hamamatsu C13272-02. As seen in Fig. (5.5). Note, that in both of the images the same colour scaling was used and the artifacts in the corners are again resulting from the aperture of the microspectrometer. Due to strong absorptions the resulting images are noisy, which can be noticed by the structure, that is visible throughout the whole picture. It is not clear, whether this structure is resulting from the combination of low intensities at the detector and the reconstruction algorithm or the structure from the cloth (see Fig.(3.12)). Structures that are present in the sample but also in the background should be neglected by the application of eq. (2.11). But due to the fact, that it is not possible to align the background and the sample cloth precisely, a superposition of cloth structures could arise. However, the stain is clearly visible and its spectrum can be extracted.

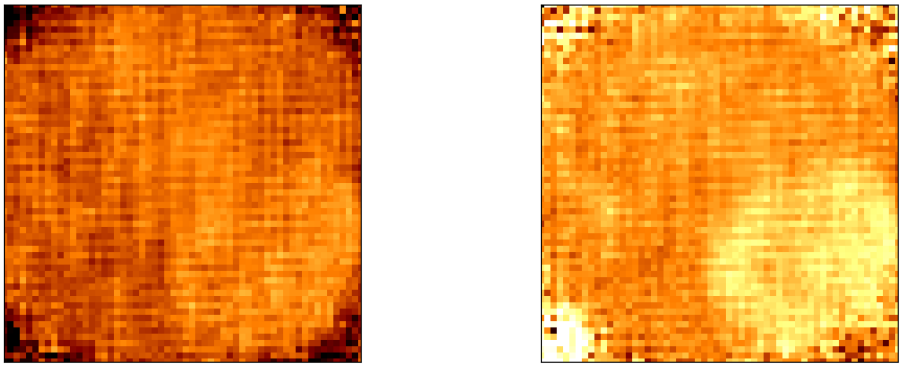

FIGURE 5.5: Left: image of a bloodstain at 1812 nm; right: same image at 1670 nm - the blood stain can clearly be seen.

The spectrum seen in Fig. (5.6) is the Savitzky-Golay filtered and baseline corrected blood spectrum extracted from the hyperspectral cube. For each wavelength the mean value of a blood containing area of 336 pixels has been computed and plotted. A prominent band centered around 1760 nm can be seen.

A further band at 1710 nm can only be assumed, but not confirmed by the data. According to [38] two bands resulting from hemoglobin overtone transitions at 1690 nm and 1740 nm should be visible. Absorbance values in this case have to be understood as mean values of $-\log(I_i/I_b)$, where I_i stands for the intensity of the pixel of the sample image and I_b stands for the pixels of the background image. It is clear, that this method of measuring a blood spectrum can lead to artifacts or spectral shifts. Nevertheless it is possible to image the bloodstain to extract a spectrum. Taking one step further this approach could be used to image blood stains and distinguish them from other kinds of stains via data analysis.

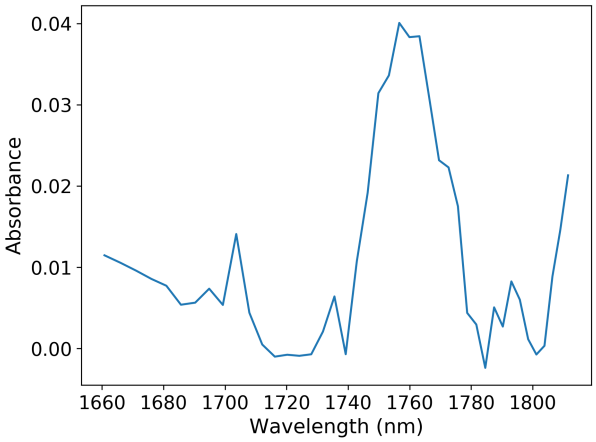

FIGURE 5.6: Absorption spectrum of blood, extracted from the hyperspectral cube.

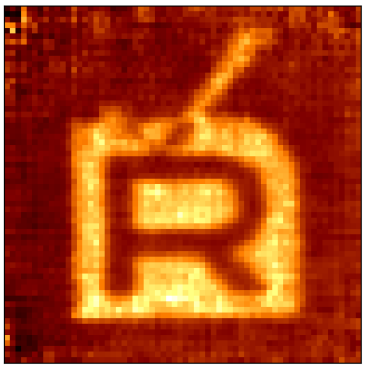

FIGURE 5.7: Absorbance image of an icon printed in black on white paper.

5.4 Measurements with a supercontinuum source

Supercontinuum sources have higher intensities, and a high spatial coherence in comparison to conventional near-infrared sources. This leads to a higher achievable SNR in a measurement. The second, shorter version of the optical setup described in chapter 3 was realized using an infrared supercontinuum source

for illumination of the sample. These measurements were performed to verify the simulations for the shorter setup. The beam of the supercontinuum source had to be expanded in order to illuminate the whole sample, thus indicating that measurements over bigger distances are possible. The setup can be seen in Fig.(3.7). The halogen light source was replaced by the supercontinuum source and instead of a microspectrometer a standard Thorlabs NIR sensitive detector was used. A bandpass filter with central wavelength of 2000 nm (bandwidth of 500 nm) had to be placed prior to the sample to prevent it from burning. In Fig.(5.7) a 64 by 64 pixel image with 60 % compression can be seen, proving that the shorter setup works in combination with a supercontinuum source.

Chapter 6

Conclusion

Aim of this work was to expand the technology of compressive hyperspectral imaging into the near infrared domain and present a cost efficient alternative to conventional hyperspectral imaging system in this domain. A broadband hyperspectral compressive imaging system was developed and constructed from scratch. Center pieces are a DMD that acts as a spatial light modulator and a Fabry-Pérot resonator based microspectrometer serving as a spectrally resolving detector. It has been shown that the system works in a wavelength domain between 1500 nm and 2200 nm, which is mainly restricted by the spectrometers that were used but also by the DMD window that protects the micromirrors. The mathematical and technical principles of hyperspectral single-pixel imaging were discussed. Simulations of two different focusing optics were presented and both were experimentally verified. The performance of the system was evaluated via dynamic range and PSNR calculations and measurements have been carried out to test the amount of compression that can be used in order to still obtain good results.
The advantage of thermal imaging over imaging in the visible range has been shown by imaging two different black markers painted on a piece of paper making the hidden marker visible due to higher absorptions in the areas where the two markers overlap. A sample with four chemically different glues on a cloth substrate has been measured at 60 different wavelengths, the respective spectra have been extracted and data analysis was performed. It was shown that the glues could be separated due to their spectral features despite scattering effects and sample imperfections. A sample of blood on black cloth was measured and the diffuse blood spectrum was extracted and compared to spectra documented in the literature. Measurements using a supercontinuum source as sample illumination have been executed, demonstrating the more compact alternative of the optical setup and comparing it to measurements with the halogen lamp as light source. It is assumed, that using the supercontinuum source in the NIR does not have a big advantage as opposed to the halogen lamp regarding image quality. But those sources could be beneficial for stand off measurements since they show a large spatial coherence.
It is clear that the current status of the near infrared hyperspectral imaging system is not fully optimized, due to the fact that the whole system is concipated as a proof of principle and there are many possibilities to expand and improve it. In the future data acquisition can be speed up drastically. With proper synchronization methods, it should be possible to achieve pattern rates of up to 650 Hz making it feasible to record images at 1 Hz rates. Hyperspectral

cubes with 60 wavelengths would then be recorded in approximately 1 min. An additional outlook is the transition into the mid infrared domain, where the whole concept of hyperspectral imaging is even more interesting due to fundamental molecular vibrations that can be exploited. Compact, robust and inexpensive hyperspectral imaging devices for the NIR and MIR will be used in various fields like quality control of food, crime investigation (blood detection) and nondestructive material testing. The use of Supercontinuum Sources could be very beneficial in the MIR wavelength domain due to big absorptions and lacking intensities of conventional mid infrared sources.

Bibliography

[1] D. Donoho, "Compressed sensing", *IEEE Transactions on Information Theory*, vol. 52, no. 4, pp. 1289–1306, 2006, ISSN: 0018-9448. DOI: 10.1109/TIT.2006.871582. [Online]. Available: http://ieeexplore.ieee.org/document/1614066/.

[2] S. B. Andersson and L. Y. Pao, "Non-raster sampling in atomic force microscopy: A compressed sensing approach", in *2012 American Control Conference (ACC)*, IEEE, 2012, pp. 2485–2490, ISBN: 978-1-4577-1096-4. DOI: 10.1109/ACC.2012.6315406. [Online]. Available: http://ieeexplore.ieee.org/document/6315406/.

[3] C. R. Berger, Z. Wang, J. Huang, and S. Zhou, "Application of compressive sensing to sparse channel estimation", *IEEE Communications Magazine*, vol. 48, no. 11, pp. 164–174, 2010, ISSN: 0163-6804. DOI: 10.1109/MCOM.2010.5621984. [Online]. Available: https://ieeexplore.ieee.org/document/5621984/.

[4] S. Qaisar, R. M. Bilal, W. Iqbal, M. Naureen, and S. Lee, "Compressive sensing: From theory to applications, a survey", *Journal of Communications and Networks*, vol. 15, no. 5, pp. 443–456, 2013, ISSN: 1229-2370. DOI: 10.1109/JCN.2013.000083. [Online]. Available: http://ieeexplore.ieee.org/document/6674179/.

[5] Y. Oiknine, I. August, D. G. Blumberg, and A. Stern, "NIR hyperspectral compressive imager based on a modified Fabry–Perot resonator", *Journal of Optics*, vol. 20, no. 4, p. 044 011, 2018, ISSN: 2040-8978. DOI: 10.1088/2040-8986/aab3b8. [Online]. Available: http://stacks.iop.org/2040-8986/20/i=4/a=044011?key=crossref.12e510fad8a63d0e5215432076ea48f3.

[6] D. Takhar, J. N. Laska, M. B. Wakin, M. F. Duarte, D. Baron, S. Sarvotham, K. F. Kelly, and R. G. Baraniuk, "A new compressive imaging camera architecture using optical-domain compression", C. A. Bouman, E. L. Miller, and I. Pollak, Eds., vol. 6065, International Society for Optics and Photonics, 2006, pp. 606 509–606509–10. DOI: 10.1117/12.659602. [Online]. Available: http://proceedings.spiedigitallibrary.org/proceeding.aspx?articleid=728899.

[7] M. F. Duarte, M. A. Davenport, D. Takhar, J. N. Laska, T. Sun, K. F. Kelly, and R. G. Baraniuk, "Single-pixel imaging via compressive sampling", *IEEE Signal Processing Magazine*, vol. 25, no. 2, pp. 83–91, 2008, ISSN: 1053-5888. DOI: 10.1109/MSP.2007.914730. [Online]. Available: http://ieeexplore.ieee.org/document/4472247/.

[8] N. Radwell, K. J. Mitchell, G. M. Gibson, M. P. Edgar, R. Bowman, and M. J. Padgett, "Single-pixel infrared and visible microscope", *Optica*, vol. 1, no. 5, p. 285, 2014, ISSN: 2334-2536. DOI: 10.1364/OPTICA.1.000285. [Online]. Available: https://www.osapublishing.org/optica/abstract.cfm?uri=optica-1-5-285.

[9] C. Brännlund and D. Gustavsson, "Single Pixel SWIR Imaging using Compressed Sensing", 2017.

[10] F. Soldevila, E. Irles, V. Durán, P. Clemente, M. Fernández-Alonso, E. Tajahuerce, and J. Lancis, "Single-pixel polarimetric imaging spectrometer by compressive sensing", *Applied Physics B*, vol. 113, no. 4, pp. 551–558, 2013, ISSN: 0946-2171. DOI: 10.1007/s00340-013-5506-2. [Online]. Available: http://link.springer.com/10.1007/s00340-013-5506-2.

[11] F. Magalhães, F. M. Araújo, M. Correia, M. Abolbashari, and F. Farahi, "High-resolution hyperspectral single-pixel imaging system based on compressive sensing", *Optical Engineering*, vol. 51, no. 7, p. 071 406, 2012, ISSN: 0091-3286. DOI: 10.1117/1.OE.51.7.071406. [Online]. Available: http://opticalengineering.spiedigitallibrary.org/article.aspx?doi=10.1117/1.OE.51.7.071406.

[12] S. Jin, W. Hui, Y. Wang, K. Huang, Q. Shi, C. Ying, D. Liu, Q. Ye, W. Zhou, and J. Tian, "Hyperspectral imaging using the single-pixel Fourier transform technique", *Scientific Reports*, vol. 7, no. 1, p. 45 209, 2017, ISSN: 2045-2322. DOI: 10.1038/srep45209.

[13] K. Shibuya, T. Minamikawa, Y. Mizutani, H. Yamamoto, K. Minoshima, T. Yasui, and T. Iwata, "Scan-less hyperspectral dual-comb single-pixel-imaging in both amplitude and phase", *Optics Express*, vol. 25, no. 18, p. 21 947, 2017, ISSN: 1094-4087. DOI: 10.1364/OE.25.021947. [Online]. Available: https://www.osapublishing.org/abstract.cfm?URI=oe-25-18-21947.

[14] Y. Zhao, N. Hu, Y. Wang, Y. Liu, X. Li, and J. Wang, "The application of near-infrared reflectance hyperspectral imaging for the detection and extraction of bloodstains", *Cluster Computing*, pp. 1–9, 2018, ISSN: 1386-7857. DOI: 10.1007/s10586-018-1869-9. [Online]. Available: http://link.springer.com/10.1007/s10586-018-1869-9.

[15] P. K. K. Hamamatsu, "InGaAs Photodiodes InGaAs Photodiodes Near infrared detectors with low noise and superb frequency characteristics", Tech. Rep. [Online]. Available: https://seltokphotonics.com/upload/iblock/20f/20f0c2052b5468672fe7009260f77823.pdf.

[16] C. E. Shannon, "Communication in the Presence of Noise Classic Paper", Tech. Rep., 1998. [Online]. Available: http://nms.csail.mit.edu/spinal/shannonpaper.pdf.

[17] E. Candes, J. Romberg, and T. Tao, "Robust uncertainty principles: exact signal reconstruction from highly incomplete frequency information", *IEEE Transactions on Information Theory*, vol. 52, no. 2, pp. 489–509, 2006, ISSN: 0018-9448. DOI: 10.1109/TIT.2005.862083.

[18] A. M. Raid, W. M. Khedr, M. A. El-Dosuky, and W. Ahmed, "Jpeg Image Compression Using Discrete Cosine Transform-A Survey", *International Journal of Computer Science & Engineering Survey (IJCSES)*, vol. 5, no. 2, 2014. DOI: 10.5121/ijcses.2014.5204. [Online]. Available: https://arxiv.org/pdf/1405.6147.pdf.

[19] R. Tibshirani, "Regression shrinkage and selection via the lasso: a retrospective", *Journal of the Royal Statistical Society: Series B (Statistical Methodology)*, vol. 73, no. 3, pp. 273–282, 2011, ISSN: 1467-9868. DOI: 10.1111/J.1467-9868.2011.00771.X@10.1111/(ISSN)1467-9868.TOP_SERIES_B_RESEARCH. [Online]. Available: https://rss.onlinelibrary.wiley.com/doi/abs/10.1111/j.1467-9868.2011.00771.x{\%}4010.1111/{\%}28ISSN{\%}291467-9868.TOP{_}SERIES{_}B{_}RESEARCH.

[20] W. Pratt, J. Kane, and H. Andrews, "Hadamard transform image coding", *Proceedings of the IEEE*, vol. 57, no. 1, pp. 58–68, 1969, ISSN: 0018-9219. DOI: 10.1109/PROC.1969.6869. [Online]. Available: http://ieeexplore.ieee.org/document/1448799/.

[21] G. Zhang, S. Jiao, and X. Xu, "Compressed sensing and reconstruction with Semi-Hadamard matrices", in *2010 2nd International Conference on Signal Processing Systems*, IEEE, 2010, pp. V1–194–V1–197, ISBN: 978-1-4244-6892-8. DOI: 10.1109/ICSPS.2010.5555570. [Online]. Available: http://ieeexplore.ieee.org/document/5555570/.

[22] E. J. Candès, "The restricted isometry property and its implications for compressed sensing", *Comptes Rendus Mathematique*, vol. 346, no. 9-10, pp. 589–592, 2008, ISSN: 1631-073X. DOI: 10.1016/J.CRMA.2008.03.014. [Online]. Available: https://www.sciencedirect.com/science/article/pii/S1631073X08000964.

[23] Scikit-learn, *3.2.4.1.3. sklearn.linear_model.LassoCV — scikit-learn 0.20.2 documentation*. [Online]. Available: https://scikit-learn.org/stable/modules/generated/sklearn.linear{_}model.LassoCV.html (visited on 02/05/2019).

[24] W. The Engineering Toolbox, *Electromagnetic Spectrum*. [Online]. Available: https://www.engineeringtoolbox.com/electromagnetic-spectrum-d{_}1929.html (visited on 02/12/2019).

[25] P. R. Griffiths and J. A. de Haseth, *Fourier Transform Infrared Spectrometry*, Second edi. John Wiley & Sons, Inc, 2007, p. 560, ISBN: 978-0-471-19404-0.

[26] Hamamatsu, *Enable real-time spectroscopic measurement at work sites and homes Ultra-Small Spectroscopic Sensor | Hamamatsu Photonics*. [Online]. Available: https://www.hamamatsu.com/eu/en/news/featured-products{_}technologies/2018/20180930000000.html (visited on 02/05/2019).

[27] P. H. C. Eilers and H. F. M. Boelens, "Baseline Correction with Asymmetric Least Squares Smoothing", 2005. [Online]. Available: https://zanran{_}storage.s3.amazonaws.com/www.science.uva.nl/ContentPages/443199618.pdf.

[28] A. Savitzky and M. J. E. Golay, "Smoothing and Differentiation of Data by Simplified Least Squares Procedures.", *Analytical Chemistry*, vol. 36, no. 8, pp. 1627–1639, 1964, ISSN: 0003-2700. DOI: 10.1021/ac60214a047. [Online]. Available: http://pubs.acs.org/doi/abs/10.1021/ac60214a047.

[29] G. James, D. Witten, T. Hastie, and R. Tibshirani, *An Introduction to Statistical Learning*, ser. Springer Texts in Statistics. New York, NY: Springer New York, 2013, vol. 103, ISBN: 978-1-4614-7137-0. DOI: 10.1007/978-1-4614-7138-7. [Online]. Available: http://www-bcf.usc.edu/{~}gareth/ISL/http://link.springer.com/10.1007/978-1-4614-7138-7.

[30] J. Demšar, T. Curk, A. Erjavec, Č. Gorup, T. Hočevar, M. Milutinovič, M. Možina, M. Polajnar, M. Toplak, A. Starič, M. Štajdohar, L. Umek, L. Žagar, J. Žbontar, M. Žitnik, and B. Zupan, "Orange: Data Mining Toolbox in Python", *Journal of Machine Learning Research*, vol. 14, pp. 2349–2353, 2013. [Online]. Available: http://jmlr.org/papers/v14/demsar13a.html.

[31] P. Gattinger, J. Kilgus, I. Zorin, G. Langer, R. Nikzad-Langerodi, C. Rankl, M. Gröschl, and M. Brandstetter, "Broadband near-infrared hyperspectral single pixel imaging for chemical characterization", *Optics Express*, vol. 27, no. 9, p. 12 666, 2019, ISSN: 1094-4087. DOI: 10.1364/OE.27.012666. [Online]. Available: https://www.osapublishing.org/abstract.cfm?URI=oe-27-9-12666.

[32] J. M. Dudley, G. Genty, and S. Coen, "Supercontinuum generation in photonic crystal fiber", 2006. DOI: 10.1103/RevModPhys.78.1135. [Online]. Available: http://image.sciencenet.cn/olddata/kexue.com.cn/upload/blog/file/2009/8/2009814185831242431.PDF.

[33] S. Dai, Y. Wang, X. Peng, P. Zhang, X. Wang, Y. Xu, S. Dai, Y. Wang, X. Peng, P. Zhang, X. Wang, and Y. Xu, "A Review of Mid-Infrared Supercontinuum Generation in Chalcogenide Glass Fibers", *Applied Sciences*, vol. 8, no. 5, p. 707, 2018, ISSN: 2076-3417. DOI: 10.3390/app8050707. [Online]. Available: http://www.mdpi.com/2076-3417/8/5/707.

[34] N. Photonics, *SuperK MIR mid IR supercontinuum laser - NKT Photonics*. [Online]. Available: https://www.nktphotonics.com/lasers-fibers/product/superk-mir-mid-ir-supercontinuum-laser/ (visited on 04/09/2019).

[35] J. Happich, *Unboxing TI's DLP LightCrafter*. [Online]. Available: https://www.eenewseurope.com/news/unboxing-tis-dlp-lightcrafter (visited on 06/26/2019).

[36] S. S. Welsh, M. P. Edgar, R. Bowman, P. Jonathan, B. Sun, and M. J. Padgett, "Fast full-color computational imaging with single-pixel detectors", *Optics Express*, vol. 21, no. 20, p. 23 068, 2013, ISSN: 1094-4087. DOI: 10.1364/OE.21.023068. [Online]. Available: https://www.osapublishing.org/oe/abstract.cfm?uri=oe-21-20-23068.

[37] J. Suo, L. Bian, Y. Xiao, Y. Wang, L. Zhang, and Q. Dai, "A self-synchronized high speed computational ghost imaging system: A leap towards dynamic capturing", *Optics & Laser Technology*, vol. 74, pp. 65–71, 2015, ISSN: 0030-3992. DOI: 10.1016/J.OPTLASTEC.2015.05.007. [Online]. Available: https://www.sciencedirect.com/science/article/pii/S0030399215001371.

[38] G. Edelman, V. Manti, S. M. Van Ruth, T. Van Leeuwen, and M. Aalders, "Identification and age estimation of blood stains on colored backgrounds by near infrared spectroscopy", 2012. DOI: 10.1016/j.forsciint.2012.03.009. [Online]. Available: https://pdf.sciencedirectassets.com/271258/1-s2.0-S0379073812X00070/1-s2.0-S0379073812001338/main.pdf.